




Article

# Effects of Tidal Stream Energy Exploitation on Estuarine Circulation and Its Seasonal Variability

Marcos Sánchez <sup>1</sup>, David Mateo Fouz <sup>1</sup> , Iván López <sup>1</sup> , Rodrigo Carballo <sup>1</sup> and Gregorio Iglesias <sup>2,3,\*</sup> 

<sup>1</sup> Departamento de Enxeñaría Agroforestal, Universidade de Santiago de Compostela, EPSE, Rúa Benigno Ledo s/n, 27002 Lugo, Spain

<sup>2</sup> MaREI, Environmental Research Institute & School of Engineering, University College Cork, P43 C573 Cork, Ireland

<sup>3</sup> School of Engineering, University of Plymouth, Plymouth PL4 8AA, UK

\* Correspondence: gregorio.iglesias@ucc.ie

**Abstract:** Residual flows are of major importance in coastal areas, driving environmental processes such as sediment transport or nutrient dispersion. Consequently, in those areas where a large tidal stream energy resource is available, prior to the installation of a tidal farm, it is imperative to assess how energy extraction affects the residual flows and, in particular, upwelling events. In this paper, the potential effects of different configurations of tidal stream farms on the residual circulation and its seasonality are analysed by means of a case study: Ria de Ortigueira, the westernmost of the Galician Rias Altas (NW Spain). For this purpose, a 3D numerical model was implemented and validated against field measurements. Next, a total of eight case studies, including the operation of bottom-fixed and floating converters under typical summer and winter scenarios, considering upwelling favourable winds, were studied. Overall, when a tidal farm operates, regardless of its configuration and the forcings considered, the resulting general residual flow pattern does not experience significant modifications. This pattern is characterized by a 2D circulation in the inner ria and a positive estuarine circulation in the middle and outer ria. The largest modifications of the residual flow are apparent in the vicinities of the plant, with maximum values of about  $0.05 \text{ ms}^{-1}$ . Outside this area, the alteration is lower than  $0.01 \text{ ms}^{-1}$  and virtually negligible at some distance from the farm where upwelling events develop.

**Keywords:** tidal stream energy exploitation; impact assessment; residual circulation; seasonal variability; upwelling; 3D numerical model



**Citation:** Sánchez, M.; Fouz, D.M.; López, I.; Carballo, R.; Iglesias, G. Effects of Tidal Stream Energy Exploitation on Estuarine Circulation and Its Seasonal Variability. *J. Mar. Sci. Eng.* **2022**, *10*, 1545. <https://doi.org/10.3390/jmse10101545>

Academic Editors: Mohamed Benbouzid and Rafael Morales

Received: 1 September 2022

Accepted: 17 October 2022

Published: 20 October 2022

**Publisher's Note:** MDPI stays neutral with regard to jurisdictional claims in published maps and institutional affiliations.



**Copyright:** © 2022 by the authors. Licensee MDPI, Basel, Switzerland. This article is an open access article distributed under the terms and conditions of the Creative Commons Attribution (CC BY) license (<https://creativecommons.org/licenses/by/4.0/>).

## 1. Introduction

The interest in carbon-free energy sources has increased drastically, resulting to a large extent from the effects of climate change, which have become more evident over the last decades [1,2]. In this context, a large number of policies have been implemented within different legal frameworks in order to achieve more ambitious quotas of renewable energy production [3–8]. In this regard, the development of new renewable energies is a key to reduce fossil fuels consumption and to fight against climate change [9]. More specifically, marine renewable energies (MRE), and in particular tidal stream energy, stand out as one of the most promising alternatives to diversify the energy mix by means of zero emission technologies, principally due to its advantages in comparison with other types of renewable energies, such as its predictability, no land occupation, or a high load factor [10–12], along with it being mature enough to be ready for its commercial development [13].

Generally speaking, tidal stream exploitation is potentially of interest in coastal areas where peak velocities exceed  $1.0\text{--}1.5 \text{ ms}^{-1}$  [14], resulting from different factors such as large tidal prisms and a constricted morphology [15,16]. These factors are sometimes reinforced by baroclinic flows and river discharges [17]. The harnessing of tidal stream energy resource is carried out through tidal energy converters (TECs), which are usually

classified according to their principle of operation as reciprocating [18] or rotating [19] devices. Rotating devices, also known as tidal stream turbines (TSTs), present the highest technology readiness level (TRL). Nowadays, third-generation TSTs [20] are designed to operate in shallow areas (approx. 1 m depth) with relatively low cut-in velocities (roughly  $0.7 \text{ ms}^{-1}$ ) [17]. TSTs can be installed in different configurations, whose influence on the performance of a tidal farm was investigated in previous works [12]. Depending on their position in the water column, TSTs may be classified as [21]: (i) floating TSTs, i.e., devices anchored to the sea bottom floating below the sea surface, which harness the energy of the upper layers of the water column, and (ii) bottom-fixed TSTs, i.e., converters rigidly anchored to the sea bottom that harness the energy available in the bottom layers of the water column.

Suitable sites for installing a tidal farm are usually located in coastal areas driven by complex hydrodynamic patterns, such as estuaries or bays, which typically have high environmental value. This highlights the key role of an appropriate environmental impact assessment for informed decision making when installing a tidal farm [22–24]. In order to investigate the impacts of tidal stream energy exploitation over estuarine circulation, both transient and residual tidal flows were analysed in previous works by means of 3D numerical modelling [25], including a comparison between floating and bottom-fixed TSTs [26]. The results demonstrate that: (i) the impacts on the residual circulation extend their effects over wider regions than in the case of transient circulation (despite being of the same order in terms of percentage of velocity variation), and (ii) there are almost no differences regarding the impact on estuarine circulation between floating and bottom-fixed configurations, with the most significant differences occurring in the vicinity of the plants, principally due to the different vertical configuration.

For all this extensive work, in areas suitable for tidal stream energy exploitation, there are other circulation patterns to be considered, e.g., upwelling-downwelling systems, which have not been well-studied in the vicinity of a tidal farm. An example of the effects of upwelling events can be found in the Galician Rias (NW Spain)—a region with one of the largest oceanic productivities worldwide [27]. Galician Rias are flooded tectonic valleys, which are usually classified into Rias Altas and Rias Baixas according to the geographical location (north and south of Cape Fisterra, respectively). There are important tectonic and geomorphological differences between both groups [28]: the Rias Baixas are larger, deeper, and more homogeneous in their orientation (roughly NE-SW) than the Rias Altas. Upwelling events throughout the Rias Baixas have been extensively analysed in the scientific literature [29–36], and their key role in cooling and fertilizing surface waters is clearly highlighted [37]. Ekman transport is the driver of upwelling processes due to the incursion of Eastern North Atlantic Central Water (ENACW) into the Rias Baixas, which usually occurs during spring or summer in the presence of N-NE winds. As a result of the orientation of these rias (NE-SW), northerly winds cause a positive estuarine circulation, which consists in an outflow in the surface layers and inflow of cold and nutrient-laden ENACW, which ascends from the continental shelf and finally flows into the ria [38–40].

The frequency and intensity of upwelling episodes are highly influenced by the orientation of the coast, which modifies the wind velocity and direction [41,42]. Several studies [27,43] remarked that the forcing factors driving the hydrodynamics in the Rias Altas are clearly dependent on the geographic orientation of a specific coastal system, as it is much more heterogeneous than in the case of the Rias Baixas. Taking this into account, and as a result of their different coastal orientation, upwelling favourable conditions along the Rias Altas are not related to the spring-summer NE winds typical of the Rias Baixas [41]. In effect, the features of the upwelling episodes along this coastal region are partially unknown, with the specific orientation of each estuary playing a significant role in the resulting hydrographical, biogeochemical, and biological patterns during upwelling and downwelling events within Rias Altas [44].

With this in view, and in order to go further into the analysis of the impacts of a tidal farm on the residual circulation and estuarine upwelling, this work studies the effects

resulting from the operation of a tidal stream plant in a specific coastal area of the Rias Altas, the Ria de Ortigueira, by means of the implementation of a 3D high-resolution hydrodynamic numerical model.

This paper is structured as follows. First, in Section 2, a brief description of the study area, the Ria de Ortigueira, is presented. Next, in Section 3, the methodology used in this work for assessing the impacts of the operation of a tidal farm on the residual circulation and estuarine upwelling is thoroughly described. Then, in Section 4, results are presented and discussed focusing on two situations: unaltered and altered conditions (i.e., without and with energy extraction, respectively). Finally, in Section 5, conclusions are drawn.

## 2. Study Area

The Ria de Ortigueira (Figure 1) is the westernmost of the Galician Rias Altas (NW Spain) delimited by Cape Ortegal and Pt. Estaca de Bares, presenting a total surface area of 85 km<sup>2</sup> and a length of 18 km along its main axis. This coastal area emerges as a promising region for tidal stream energy exploitation thanks to its complex geomorphology, with a number of constrictions, and its relatively high tidal range (maxima of 4.5 m). Previous works [16,45] show that tidal flows of approximately 2.5 ms<sup>-1</sup> can be reached in the narrowing between Pt. Postiña and Pt. Cabalar, indicating the suitability of the Ria de Ortigueira as the location for a tidal stream farm.

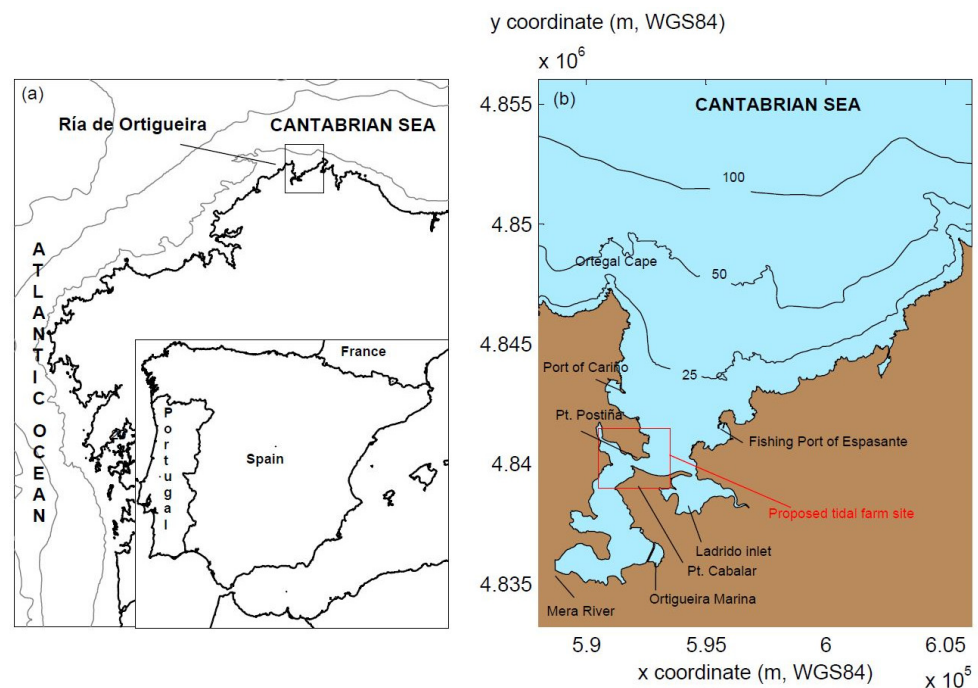


**Figure 1.** The Ria de Ortigueira (b) and its location in Galicia (NW Spain) (a).

Regarding the tidal regime of the Ria de Ortigueira, it is characterized by a predominance of semidiurnal components (Table 1), especially M2, as in the rest of the European Atlantic. In this regard, considering the main tidal constituents (M2, S2, K1, and O1) by means of a harmonic analysis, the tidal form factor ( $F$ ) confirms the semidiurnal behaviour ( $F = 0.082$ ) of this body of water [46]. In this Ria, the action of the tide is highly modified by its main geomorphological features. Ria de Ortigueira presents a gradual reduction in the width of its cross-sections from the mouth to the inner ria, ranging from more than 10 km at its ocean boundary to 150–200 m in the inner estuary. As far as the water depth is concerned, it presents an average value of 7.3 m [47] but with strong variations throughout the estuary, varying from maximums of 30–35 m at its mouth to less than 5 m throughout extensive zones in the inner ria, including large intertidal areas.

**Table 1.** Main tidal constituents in the Ria de Ortigueira.

Constituent	Amplitude (cm)	Phase (°)
M2	122.79	90.15
S2	42.91	121.08
N2	25.98	70.39
K2	12.03	118.76
K1	7.35	73.49
O1	6.22	324.62
P1	2.22	65.15
Q1	2.11	271.31
M4	1.45	334.80

Even though that the hydrodynamics of the Ria de Ortigueira are dominated by the tide, tides are not the only relevant forcing factor within this estuarine area, such as: (i) fluvial discharges, (ii) thermohaline conditions, and (iii) wind regime. As a result of the interaction of the different forcing factors driving the hydrodynamics of the Ria de Ortigueira, this coastal location can be classified according to the salinity structure criterion as a well-mixed estuary [16].

Regarding fluvial discharges, though there are several fluvial courses flowing into this estuary, only the River Mera presents a significant flow rate (i.e., average annual discharge of  $5.45 \text{ m}^3 \text{ s}^{-1}$ ) to be considered as a relevant hydrodynamics forcing agent in this coastal area. A seasonal analysis [17] considering mean monthly flow rates since 1970 shows that a marked intra-annual discharge variability is apparent, resulting in two different periods (autumn–winter and spring–summer) within the hydrological year. The average characteristics of fluvial discharges and thermohaline conditions of oceanic waters for these two periods are shown in Table 2.

**Table 2.** Average values of river discharges and thermohaline conditions during spring–summer and autumn–winter scenarios.

Scenario	River Discharge Conditions			Oceanic Conditions	
	River Flow ( $\text{m}^3 \text{ s}^{-1}$ )	Salinity (ppt)	Temperature (°C)	Salinity (ppt)	Temperature (°C)
Spring–summer	3.07	0.051	15.60	35.68	15.51
Autumn–winter	8.48	0.051	11.10	35.48	13.17

With respect to the wind regime, pronounced patterns of seasonality are found again, as in the case of river discharges, and in line with other Galician Rias [48,49]: (i) autumn–winter scenario (prevalence of W-SW winds) and (ii) spring–summer scenario (prevalence of NE winds), hereinafter referred to for simplicity as winter and summer winds, respectively. Moreover, as mentioned in Section 1, in the Rias Altas the coastal orientation determines which wind directions produce upwelling flows. Considering the orientation of the shoreline in the Ria de Ortigueira (SSW–NNE), and despite NE winds being prevalent during spring–summer (upwelling favourable periods in other Galician Rias), SW winds are responsible for upwelling processes within this waterbody during both winter and summer scenarios. Upwelling episodes take place mainly during spring or summer; notwithstanding, they also occur during autumn or winter in both Rias Baixas [31] and Rias Altas [50].

### 3. Materials and Methods

#### 3.1. Numerical Model (I): Equations

With the aim of analysing the impacts of tidal stream energy exploitation on the hydrodynamics of the Ria de Ortigueira, and more specifically on the upwelling events, the 3D hydrodynamic model Delft3D-FLOW was implemented in this estuarine area. Delft3D-

FLOW approximates by means of a finite-difference code, the Navier Stokes equations (under the shallow-water and Boussinesq assumptions) combined with the transport equation, allowed the computation of both the baroclinic and barotropic circulation [51]. In order to fully describe the resulting 3D flow structure during upwelling events [40] and how a tidal farm affects them, the numerical model was implemented in its 3D form. The model equations read:

$$\frac{\partial u}{\partial x} + \frac{\partial v}{\partial y} + \frac{\partial w}{\partial z} = Q \tag{1}$$

$$\left. \begin{aligned} \frac{Du}{Dt} &= fv - g \frac{\partial \zeta}{\partial x} - \frac{g}{\rho_0} \int_{z'=z}^{z'=\zeta} \frac{\partial \rho}{\partial x} dz' + v_h \left( \frac{\partial^2 u}{\partial x^2} + \frac{\partial^2 u}{\partial y^2} \right) + v_v \left( \frac{\partial^2 u}{\partial z^2} \right) \\ \frac{Dv}{Dt} &= -fu - g \frac{\partial \zeta}{\partial y} - \frac{g}{\rho_0} \int_{z'=z}^{z'=\zeta} \frac{\partial \rho}{\partial y} dz' + v_h \left( \frac{\partial^2 v}{\partial x^2} + \frac{\partial^2 v}{\partial y^2} \right) + v_v \left( \frac{\partial^2 v}{\partial z^2} \right) \end{aligned} \right\} \tag{2}$$

$$\frac{\partial p}{\partial z} = -\rho g \tag{3}$$

$$\frac{Dc}{Dt} = D_h \left( \frac{\partial^2 c}{\partial x^2} + \frac{\partial^2 c}{\partial y^2} \right) + D_v \frac{\partial^2 c}{\partial z^2} - \lambda_d c + R_s \tag{4}$$

Equation (1) represents the conservation of mass under the assumption of incompressibility (Boussinesq assumption); Equation (2) expresses the conservation of the momentum along *x*- and *y*-directions; Equation (3) represents the conservation of the momentum in the *z*-direction, which is simplified to the hydrostatic pressure distribution according to the shallow-water assumption; lastly, Equation (4) stands for the transport equation, which is solved for salinity and temperature constituents. In these equations, *u*, *v*, and *w* are the velocity components in the *x*-, *y*-, and *z*-directions, respectively; *Q* stands for the mass source intensity per unit area; *t* is the time; *f* represents the Coriolis parameter; *g* is the gravitational acceleration ( $\approx 9.81 \text{ ms}^{-2}$ );  $\zeta$  stands for the free surface elevation relative to  $z = 0$ , i.e., the water level;  $\rho_0$  and  $\rho$  represent the reference density of sea water and the density, respectively;  $v_h$  and  $v_v$  represent the horizontal and vertical eddy viscosities, respectively;  $D_h$  and  $D_v$  stand for the horizontal and vertical eddy diffusivities, respectively; *c* represents the thermohaline conditions (i.e., salinity or temperature);  $\lambda_d$  stands for decay processes; finally,  $R_s$  is the source term per unit area.

### 3.2. Numerical Model (II): Implementation

The numerical model covers the whole ria by means of a Cartesian grid extending towards the adjacent continental shelf up to the 150 m isobath at a distance of approx. 10 km offshore. This grid (Figure 2) is composed of 57,361 varying-size cells, with the grid size set as follows: in the inner and middle ria, a grid resolution of  $50 \times 50$  m is adopted, progressively decreasing in the *y*-direction up to  $50 \times 150$  m at the outer ria (northern boundary of the grid). Regarding the vertical discretisation, a  $\sigma$ -coordinate system composed of twelve layers was used [52], with the following layer thicknesses (percentages of water column) from surface to bottom: 2, 3, 5, 10, 15, 15, 15, 10, 5, 3, and 2 [23,40,53]. This distribution of  $\sigma$ -layers, which provides a higher grid resolution near the surface and seabed, ensures an adequate modelling of boundary layer flows [53].

The bathymetric data of the Ria de Ortigueira and its surroundings were obtained from nautical charts #408 and #4083 from the Navy’s Hydrographic Institute (Instituto Hidrográfico de la Marina). Additionally, intertidal areas are fully described by using data from a  $10 \times 10$  m resolution digital elevation model.

The initial conditions for the hydrodynamic numerical model are null free-surface elevation and velocity at each node of the computational grid (cold start) [54]. As far as the transport model is concerned, the initial thermohaline conditions were prescribed at the oceanic boundaries through field measurements (the reader is referred to Table 2 for a better understanding). Moreover, in order to avoid the influence of the initial conditions on the numerical results, a 30-day spin-up period was adopted to ensure their dynamical adjustment with the flow field [35,55].



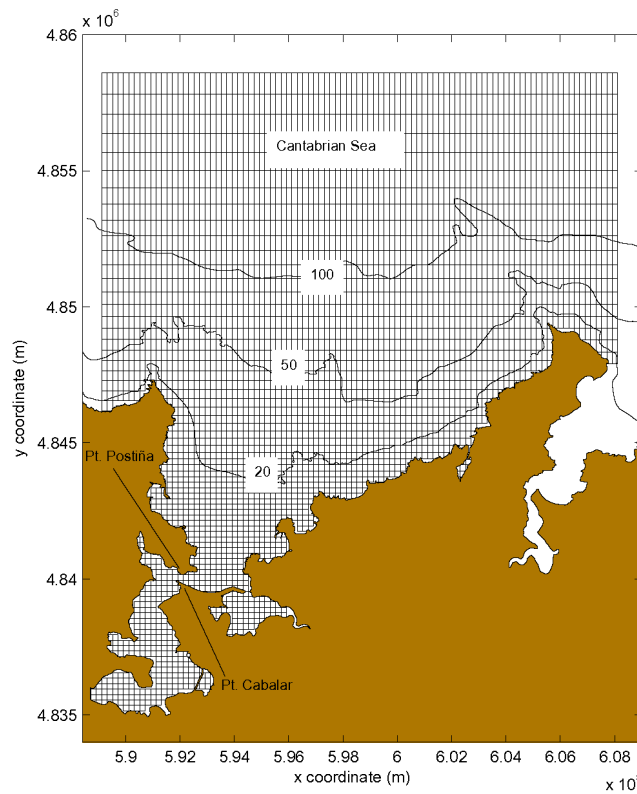


Figure 2. Numerical model grid.

Regarding the open boundary conditions, Dirichlet-type conditions were imposed along the oceanic boundaries by considering the M2 constituent and the thermohaline conditions (Table 2). At the land–water transition, null flow through the boundary and zero shear stress were imposed. At the sea bottom boundary, the shear stress,  $\vec{\tau}_{b3D}$ , induced by a turbulent flow was computed by means of a quadratic law:

$$\vec{\tau}_{b3D} = \frac{g\rho_0|\vec{u}_b|\vec{u}_b}{C_{3D}^2}, \tag{5}$$

where  $\vec{u}_b$  represents the magnitude of the horizontal velocity in the bottom layer, and  $C_{3D}$  represents the 3D Chézy coefficient, which is computed as:

$$C_{3D} = C_{2D} + \frac{\sqrt{g}}{\kappa} \ln\left(\frac{\Delta z_b}{2H}\right), \tag{6}$$

with  $k$  as the von Karman constant ( $k = 0.41$ ),  $\Delta z_b$  the distance from the sea bottom to the nearest grid node,  $H$  the water depth, and  $C_{2D}$  the 2D Chézy coefficient, which can be expressed as:

$$C_{2D} = \frac{\sqrt[6]{H}}{n}, \tag{7}$$

where  $n$  stands for the Manning’s coefficient, which is prescribed in this work as a function of the water depth [56] in order to consider the full influence of the water depth on the seabed stress [57,58].

Finally, the wind shear stress,  $\vec{\tau}_s$ , at the free surface is given by:

$$\vec{\tau}_s = \rho_a C_d |\vec{U}_{10}| \vec{U}_{10}, \tag{8}$$

where  $\rho_a$  represents the density of the air,  $\vec{U}_{10}$  stands for the wind velocity vector at 10 m height above the sea surface, and  $C_d$  is the wind drag coefficient computed following [59,60]. Moreover, regarding the main numerical and physical parameters of the numerical model, the horizontal advection terms in Equation (2) are calculated using the cyclic method [61]; as regards the temporal discretisation, the model resorts to an alternating direction implicit (ADI) algorithm [62]; finally, the  $k-\epsilon$  model was adopted for the turbulence closure [63].

The numerical model was successfully validated against field measurements obtained by means of an ADCP (Acoustic Doppler Current Profiler) and a tidal gauge deployed at two different locations in the inner and middle ria during a 19-day period. During this period, the model was forced along the oceanic boundaries with the main tidal harmonics, thermohaline conditions, wind velocity and direction and fluvial discharges of River Mera. A good agreement between computed and observed series (for both water levels and velocities) was obtained, reaching high values of the correlation coefficient  $R$  (i.e.,  $R \approx 0.99$  for water levels and  $R > 0.82$  for flow magnitude and direction at each layer) and low values of several statistical coefficients (i.e., mean difference,  $MD$ , and mean square error,  $MSE$ ). For further details of the numerical model validation, the reader is referred to previous works [12,25,26].

The implementation of the TSTs in the numerical model was conducted through the so-called momentum sink approach [22,23,64]. It consists of introducing a momentum sink term into the right-hand side of Equation (2) by means of a retarding force, which compensates the thrust force exerted by the flow on the TST [65]. Considering this, the momentum sinks can be modelled as follows:

$$\left. \begin{aligned} M_x &= \frac{F_x}{\rho} \\ M_y &= \frac{F_y}{\rho} \end{aligned} \right\} \tag{9}$$

with  $F_x$  and  $F_y$  as the components of the retarding force per unit volume  $V$  along  $x$ - and  $y$ -directions, respectively. These components are opposite and equal to the thrust force, and therefore, they can be expressed as:

$$\left. \begin{aligned} M_x &= -\frac{1}{2} \frac{C_T A}{V} U u \\ M_y &= -\frac{1}{2} \frac{C_T A}{V} U v \end{aligned} \right\} \tag{10}$$

where  $A$  represents the cross-section of a TST,  $U$  stands for the magnitude of the flow velocity, and  $C_T$  is the thrust coefficient [66]. The retarding force is considered in the vertical model layers, which correspond with the water depth at which they operate. It is important to note that the methodology applied in this study provides accurate results when analysing the modifications in the general circulation patterns considering the type of model implemented (shallow water models) and grid resolution. However, an accurate near-field analysis should resort to the implementation of high-resolution CFD (Computational Fluid Dynamics) models solving RANS (Reynolds Averaged Navier Stokes) equations.

Figure 3 shows the layout of the proposed tidal farms, which are located in the surroundings of the narrowing between Pt. Postiña and Pt. Cabalar, where the strongest tidal currents are found (see Section 1). Both plants have the same layout with a surface area of about 1500 m<sup>2</sup>. The first plant is composed of floating TSTs occupying the upper part of the water column, and the second plant is composed of TSTs of the same characteristics but fixed to the bottom and occupying the lower part of the water column.

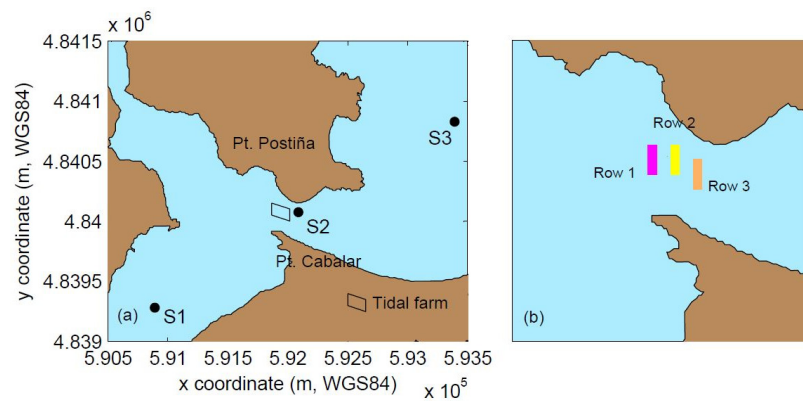


**Figure 3.** Location of the considered tidal stream plant, indicating the locations (S1, S2, and S3) for velocity and salinity profiles (a). Layout in plan view of the plants (b).

The TST selected is an Evopod turbine in view of its appropriateness for shallow waters areas [12,26,67], as is the case of the proposed location in the Ria de Ortigueira. Following the distance recommendations between lines of TSTs [68], 30 turbines with a sweep area of approx. 600 m<sup>2</sup> were distributed over three lines roughly perpendicular to the main flow direction, allowing their operation in a rather similar water depth. The technical characteristics of the Evopod turbine are provided in Table 3.

**Table 3.** Technical specifications of the Evopod turbine as provided by its developer (rotor diameter ( $D$ ), cut-in velocity ( $V_{ci}$ ), rated velocity ( $V_r$ ), cut-of velocity ( $V_{co}$ ), swept area ( $A$ ), rated power ( $P_r$ ), power coefficient in normal operation ( $C_{pNO}$ ), and power coefficient in stall control ( $C_{pSC}$ )).

$D$ (m)	$V_{ci}$ (ms <sup>-1</sup> )	$V_r$ (ms <sup>-1</sup> )	$V_{co}$ (ms <sup>-1</sup> )	$A$ (m <sup>2</sup> )	$P_r$ (kW)	$C_{pNO}$	$C_{pSC}$
5	0.7	2.2	3.1	19.6	40	0.35	0.2

### 3.3. Tide-Driven Residual Circulation

The most usual procedure to compute the residual circulation induced by the tide consists of time-averaging or filtering the transient velocities computed by the numerical model [69]. There are other approaches, such as those based on the numerical solving of the so-called residual velocity evolution equations [70], which are not considered in the present application. The transient Eulerian horizontal velocity vector numerically computed ( $u, v$ ) is decomposed into its periodic and residual components ( $u_p, v_p$ ) and ( $u_r, v_r$ ), respectively, as follows:

$$(u, v) = (u_p, v_p) + (u_r, v_r), \tag{11}$$

with the residual velocity vector computed as:

$$(u_r, v_r) = \frac{1}{T} \int_{-T/2}^{T/2} (u, v) dt, \tag{12}$$

where  $T$  represents the cut-off period of the averaging operator. A value of 12 h 25 min was adopted for this cut-off period in order to fully filter the variability of the semidiurnal tide prescribed by the dominance of the M2 tidal constituent.

### 3.4. Case Studies

In this work, a detailed assessment of the impacts of tidal stream energy exploitation on the residual circulation and estuarine upwelling was conducted following a seasonal approach. To this end, several case studies (CS) were undertaken with the aim of comparing the differences between altered and unaltered conditions (i.e., with and without energy extraction, respectively). Based on available data (Section 2), autumn–winter and spring–summer scenarios were defined, considering typical characteristics of their forcing factors.



First, the tide is introduced by considering its major semidiurnal component (M2). Second, fluvial discharges and thermohaline conditions correspond with those established in Table 2. Finally, the average value of SW winds is considered. The combinations of forcings leads to a total of eight different case studies, which are summarized in Table 4.

**Table 4.** Summary of boundary conditions and the situations simulated in the different case studies analysed.

Case Study	Tidal Plant	Wind	Fluvial and Oceanic Conditions (Table 2)
CS1	No plant	No wind	Spring–summer
CS2	No plant	No wind	Autumn–winter
CS3	No plant	SW mean summer wind (3.32 ms <sup>-1</sup> )	Spring–summer
CS4	No plant	SW mean winter wind (6.03 ms <sup>-1</sup> )	Autumn–winter
CS5	Floating plant	No wind	Autumn–winter
CS6	Bottom plant	No wind	Autumn–winter
CS7	Floating plant	SW mean winter wind (6.03 ms <sup>-1</sup> )	Autumn–winter
CS8	Bottom plant	SW mean winter wind (6.03 ms <sup>-1</sup> )	Autumn–winter

## 4. Results and Discussion

### 4.1. Unaltered Conditions

Unaltered hydrodynamic conditions (i.e., without considering energy extraction) in the Ria de Ortigueira were analysed through four case studies (CS1 to CS4), focusing this analysis on how the seasonality of river discharges and thermohaline conditions, in conjunction with the circulation induced by upwelling favourable SW winds, influence the estuarine residual circulation. With this aim, the results are provided in terms of the vectorial distribution (vector) and magnitude (colour map) of the unaltered residual circulation patterns throughout the estuary.

CS1 describes the residual circulation within the Ria de Ortigueira under summer conditions for fluvial discharges and thermohaline conditions in the absence of winds. Figure 4 shows the resulting unaltered residual circulation patterns in surface and bottom layers of the numerical grid. Two regions can be distinguished in terms of residual circulation patterns. In the inner ria (i), similar hydrodynamic patterns (i.e., a marked outflow) are present throughout the whole water column, including also a vortex rotating counterclockwise, with somewhat stronger flow velocities in surface layers (with peak velocities located in the surroundings of the narrowing between Pt. Postiña and Pt. Cabalar of about 0.20 ms<sup>-1</sup> and 0.15 ms<sup>-1</sup> in surface and bottom layers, respectively). On the other hand, the middle and outer ria (ii) are characterized by typical patterns of a positive estuarine circulation (i.e., inflow on the bottom layer and outflow on the surface layer) driven from river discharges flowing out in the surface layers.

Regarding CS2, the same forcing factors as CS1 were considered but now under winter conditions (Figure 5). As a result, the induced circulation is similar in both case studies, with somewhat greater velocities in the surface layer in the case of CS2, in particular in the middle and outer ria, due to the larger fluvial discharges. Therefore, it can be concluded that, in the absence of winds, the seasonality of the hydrodynamic driving agents does not lead to significant variations in the residual circulation of the Ria de Ortigueira as a consequence of the typical low riverine inputs to this estuary.

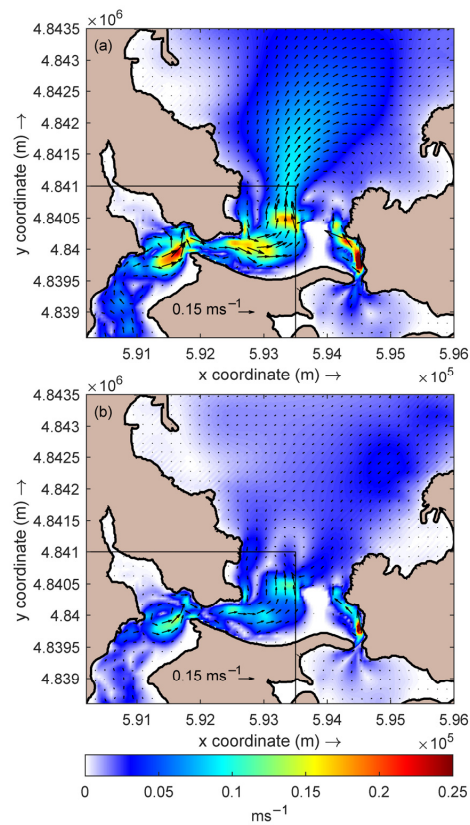


**Figure 4.** Residual flow pattern in Ria de Ortigueira under case study CS1 conditions. (a) Surface layer; (b) bottom layer.

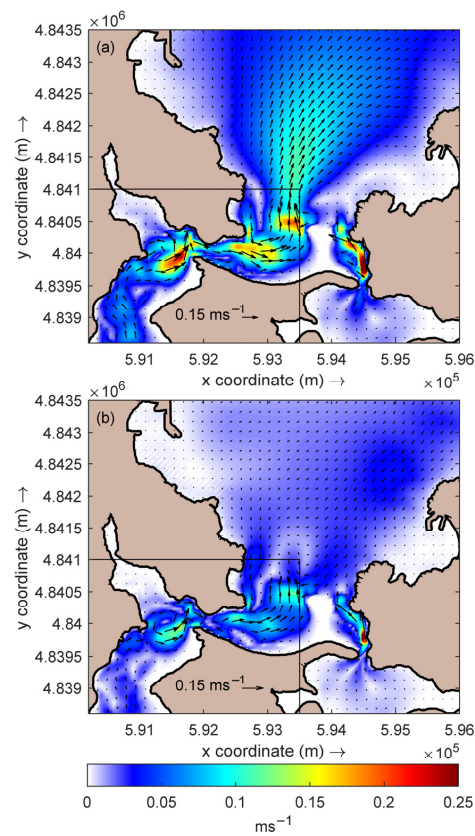


**Figure 5.** Residual flow pattern in Ria de Ortigueira under case study CS2 conditions. (a) Surface layer; (b) bottom layer.

The influence of river discharges driving the residual circulation in the inner part of the Ria can be further studied by analysing the vertical distribution of salinity at specific sites of interest, namely S1, S2, and S3 (Figure 3) in CS1 (spring–summer with no wind) and CS2 (autumn–winter) (Figure 6). It can be observed that this area can be considered as well-mixed throughout the whole year (autumn–winter and spring–summer scenarios), with virtual no differences in salinity throughout the vertical at S1 and S2 although with variations between seasons provoked by the different river discharges and oceanic thermohaline conditions (a greater fluvial discharge during winter reduces the salinity). This is the result of the large capacity of the tide (large tidal range in a shallow water area) to mix the overall low river discharges in this area. The capacity of the tide to mix the riverine and oceanic waters diminishes in the middle and outer ria, as the water depth and cross-sections increase, as it is apparent in S3.

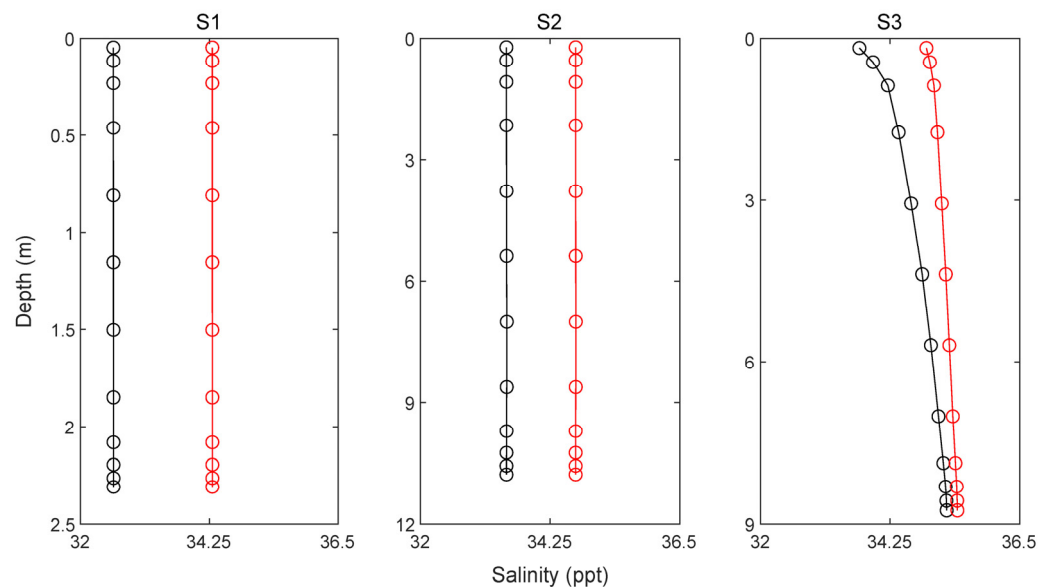


**Figure 6.** Salinity vertical profiles at S1, S2, and S3 during CS1 (spring–summer season) (red line) and CS2 (autumn–winter season) (black line).

The resulting low capacity of the river discharges generating residual currents is apparent in Figure 7, showing the vertical distribution of the residual circulation at S1, S2, and S3 in CS1 and CS2. The increase in discharge in the autumn–winter season is not capable of provoking significant greater residual velocities.

With respect to CS3, it corresponds to CS1 (i.e., summer conditions) but considering the action of the summer SW wind. The resulting circulation (Figure 8) could be characterized as a conventional two-layer estuarine circulation, reinforcing the residual patterns described in CS1 and CS2. In this case, the wind-induced outflow in the surface layer is strengthened, attaining values of about  $0.25 \text{ ms}^{-1}$  in the inner ria in the surroundings of the narrowing between Pt. Postiña and Pt. Cabalar and increasing the shelf-water intrusion through the bottom layers. Finally, it is worthy of mention that surface water masses tend to leave the ria next to its right margin. This pattern, which is also apparent although with less intensity in CS1 and CS2, is probably the result of wind action reinforced by the river discharges, which tend to deviate the flow to the right margin of the estuary as a consequence of the Coriolis force in the Northern Hemisphere.

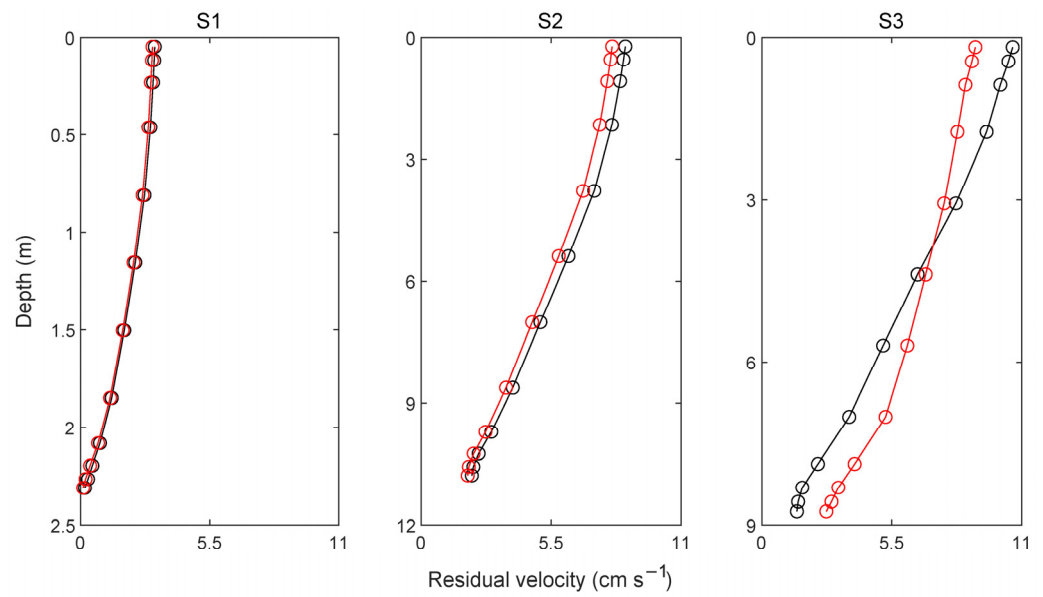


**Figure 7.** Vertical profiles of the magnitude of the residual circulation at S1, S2, and S3 during CS1 (spring–summer season) (red line) and CS2 (autumn–winter season) (black line).

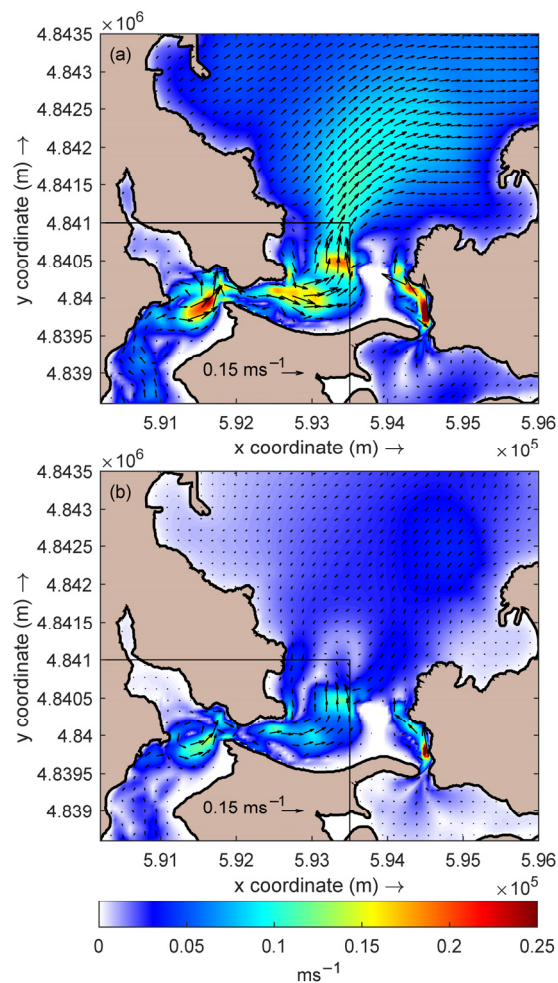


**Figure 8.** Residual flow pattern in Ria de Ortigueira under case study CS3 conditions. (a) Surface layer; (b) bottom layer.

As far as CS4 is concerned, it considers the same forcing factors as in the case of CS3 but under the action of a winter SW wind. The results obtained (Figure 9) are similar to those obtained in CS3 (Figure 8). However, due to the larger wind velocity and fluvial discharges under winter conditions, the residual currents induced in CS4 are stronger than in CS3, in particular in the surface layer, which is more influenced by wind action and river discharges, reaching values of up to  $0.25 \text{ ms}^{-1}$ .

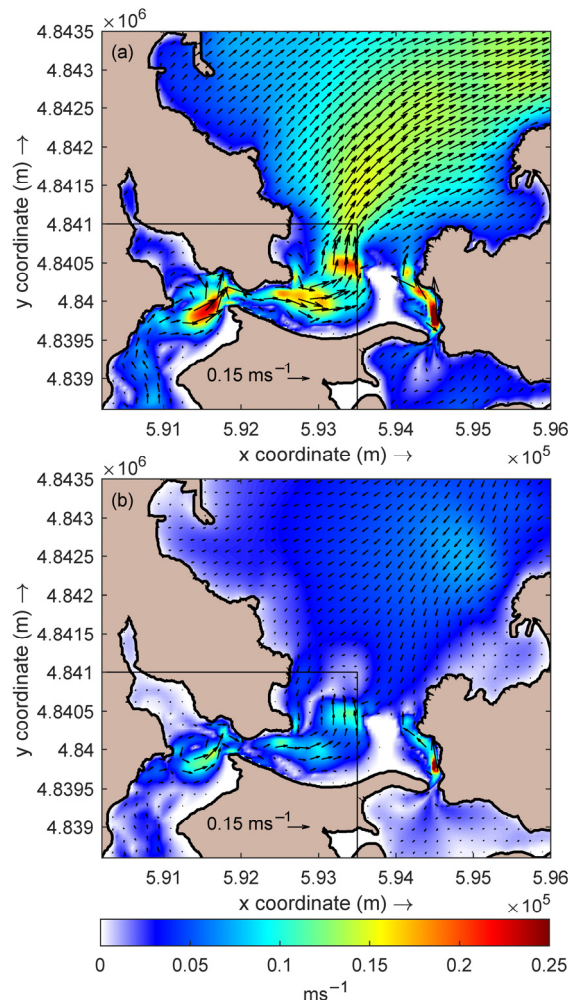


**Figure 9.** Residual flow pattern in Ria de Ortigueira under case study CS5 conditions. (a) Surface layer; (b) bottom layer.

Overall, the aforementioned comparison of the case studies corresponding to unaltered conditions (CS1 to CS4) shows how the typical low fluvial inputs discharging into the Ria de Ortigueira are not capable of inducing significant residual currents; on the contrary, the seasonality of the wind regime plays a key role in the residual circulation within this semi-enclosed waterbody.

#### 4.2. Altered Conditions

The altered hydrodynamic conditions (i.e., considering energy extraction) in the Ria de Ortigueira that would result from the operation of a tidal farm were analysed through four additional case studies (CS5 to CS8), which consider different configurations (i.e., floating and bottom-fixed converters). As a consequence of the results provided by CS1 to CS4, which show the limited effects of the seasonality of thermohaline conditions and fluvial discharges on the resulting residual patterns, CS5 to CS8 only consider typical winter thermohaline and riverine conditions (summer scenarios are not retained) under no wind action and upwelling favourable winds.



With the aim of assessing the impacts of the energy extraction, the results are provided through a comparison with unaltered conditions case studies. In this way, the results provided by CS5 to CS8 (Figures 10–13) show the vectorial distribution of the altered residual circulation patterns (vectors) and the differences in the magnitude of the residual currents between altered and unaltered conditions (colormap) in the coastal area close to the location proposed for tidal energy exploitation (Figures 4, 5, 8 and 9).

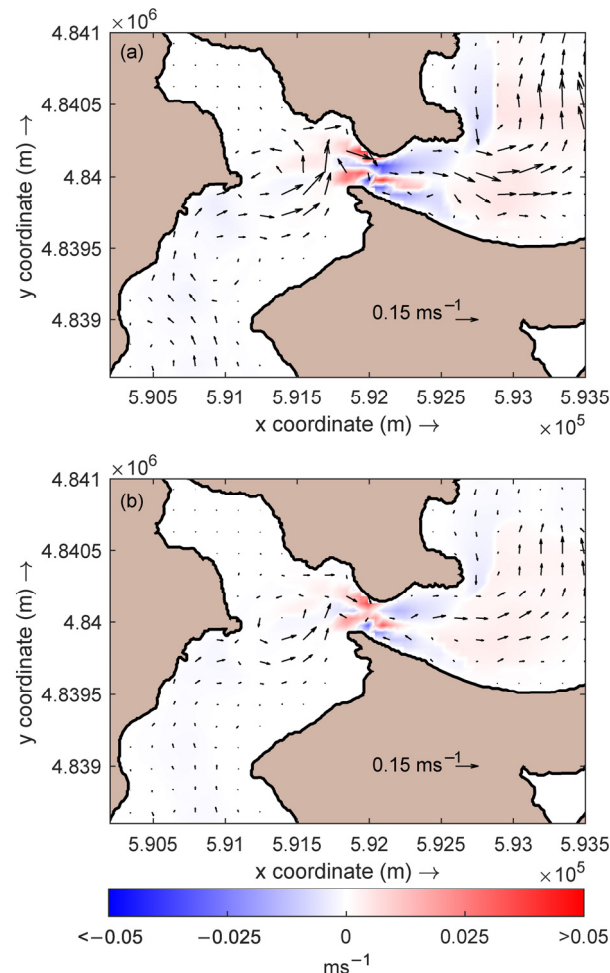


**Figure 10.** Residual flow pattern in Ria de Ortigueira under case study CS5 conditions (vectors); differences in the residual flow magnitude between altered flow and reference situation (CS5–CS2) (colour map). (a) Surface layer; (b) bottom layer.

CS5 computes the altered residual circulation within the study area considering winter thermohaline and riverine conditions in absence of winds. Regarding the implementation of the tidal farm and its energy extraction in the numerical model, it is conducted by considering a floating tidal farm, i.e., operating in the upper  $\sigma$ -layers of the grid. The results provided by CS5 (Figure 10) show that the major changes in the residual velocities are located in the constriction between Pt. Postiña and Pt. Cabalar as a consequence of the location of the proposed farm (Figure 3). Resulting from the layout of the tidal farm, which is distributed in three different lines along a W-E axis, the changes in the residual velocities along this section are spatially distributed as follows: (i) in the westernmost part of the constriction, in the surroundings of row 1, there is an apparent increase in the residual velocities towards the N and S margins of the ria for both surface and bottom layers, attaining maximum increments up to 0.05 ms<sup>-1</sup> in the case of the surface layer, where the differences between unaltered and altered conditions are somewhat higher; (ii) in the central section of the constriction, in the surroundings of row 2, the situation is not homogenous, combining residual velocity increments (roughly 0.02–0.03 ms<sup>-1</sup>) with



weaker decrements ( $0.01\text{--}0.02\text{ ms}^{-1}$ ) located W and E of row 2, respectively; finally, (iii) in the easternmost part of the constriction, in the surroundings of row 3, decrements towards the N (surface and bottom layers) and S margins (primarily in the surface layer) of the ria are apparent, along with a remarkable increase in the residual velocity within the central channel of this section (attaining maximum figures of approx.  $0.05\text{ ms}^{-1}$ ). Finally, the maximum residual velocities are of the same order than in the case of the unaltered conditions, roughly  $0.25\text{ ms}^{-1}$ .

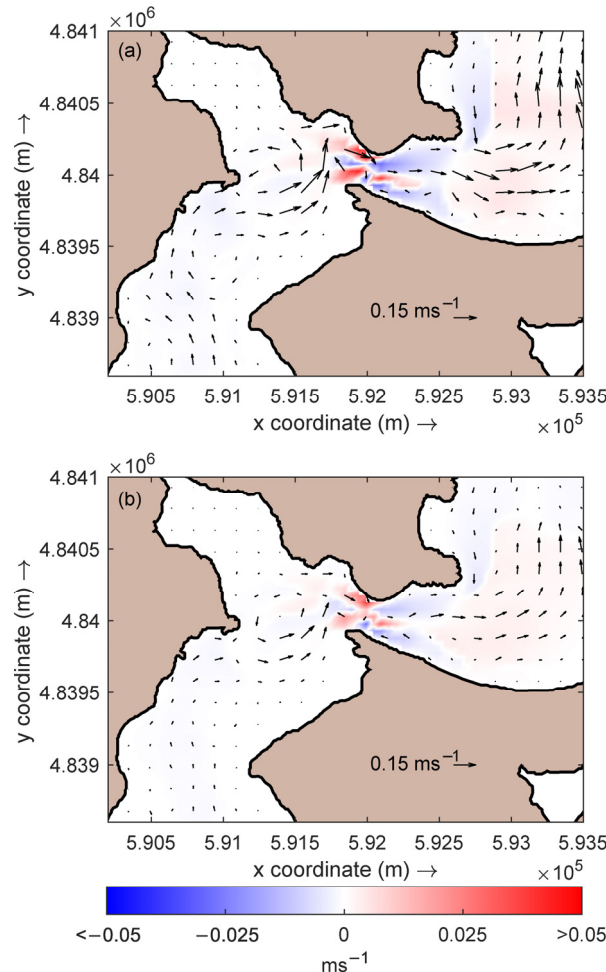


**Figure 11.** Residual flow pattern in Ria de Ortigueira under case study CS6 conditions (vectors); differences in the residual flow magnitude between altered flow and reference situation (CS6–CS2) (colour map). (a) Surface layer; (b) bottom layer.

In CS6, the same forcing factors and conditions as in the case of CS5 (winter thermohaline and riverine conditions in absence of winds) were input to the model but now considering a bottom-fixed tidal farm, i.e., operating in the lower  $\sigma$ -layers of the grid (Figure 11). The results show similar hydrodynamic patterns as in the case of the floating farm in CS5. With respect to the differences between unaltered and altered conditions, the spatial distribution of the effects of the energy extraction corresponds, in general, with those exposed in the case of CS5 (Figure 10); however, several peculiarities are now apparent: on the surface layer, the increments and decrements in the residual velocities are slightly stronger and weaker, respectively; on the contrary, on the bottom layer, the situation is roughly the opposite although with even less differences with respect to CS5. Moreover, as Figure 11 shows, there is an apparent decrement in the residual velocity (approx.  $0.02\text{ ms}^{-1}$ ) located in the surroundings of row 1, more specifically in the central channel of the ria, which is not present in the case of a floating plant.

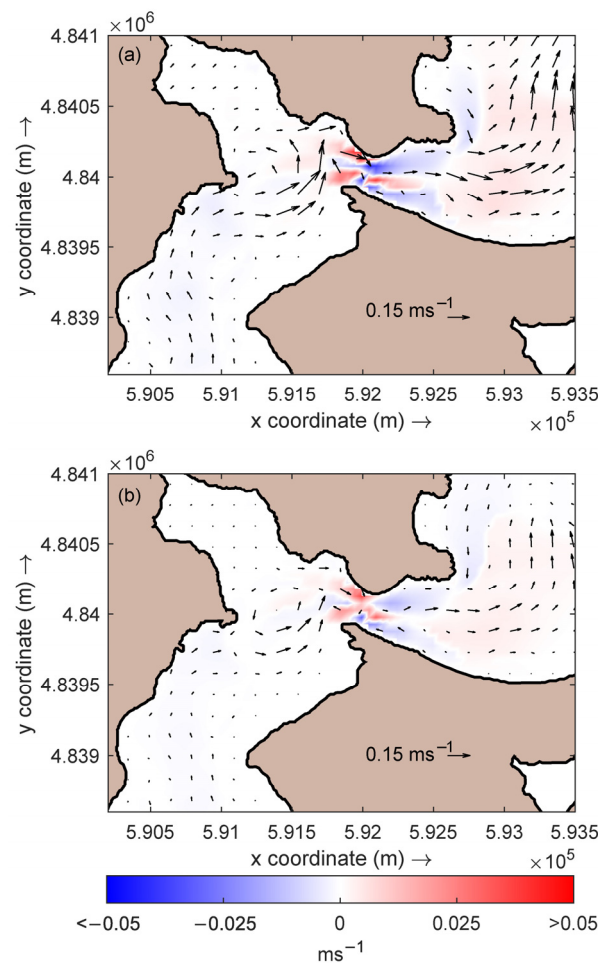


**Figure 12.** Residual flow pattern in Ria de Ortigueira under case study CS7 conditions (vectors); differences in the residual flow magnitude between altered flow and reference situation (CS7–CS4) (colour map). (a) Surface layer; (b) bottom layer.

As far as CS7 is concerned, winter thermohaline and riverine conditions were considered under the action of SW upwelling favourable winds. Likewise, the effects of the energy extraction were modelled by means of a floating tidal farm as in the case of CS5. The results of CS7 (Figure 12) show the influence of SW winds on the surface layers, in which greater outflow residual velocities are attained (i.e., close to the maximum figures of about 0.25 ms<sup>-1</sup>) in comparison with previous altered conditions case studies in absence of winds. In the same way, bottom layers also present outflow residual flows throughout the inner ria although with weak residual velocity magnitudes. Regarding the spatial distribution of the impacts generated by the energy extraction in the vicinities of the farm, CS7 presents a similar pattern along the W–E axis, as in the case of CS5 and CS6: (i) in the surroundings of row 1, there are two major areas, located towards the N and S margin of the channel, in which the greatest increase in the residual velocities (i.e., 0.03–0.04 ms<sup>-1</sup>) for both surface and bottom layers is apparent; (ii) in the surroundings of row 2, there exist several areas characterized by increments (0.02–0.03 ms<sup>-1</sup>) and decrements (0.01–0.02 ms<sup>-1</sup>) in the residual velocities W and E of row 2, respectively; finally, (iii) in the surroundings of row 3, the largest reductions in the residual velocities are located within two major areas towards the N (surface and bottom layer) and S (surface layer) margin of the ria; on the contrary, the maximum increments in the residual velocities (0.04 ms<sup>-1</sup>) are located within the central channel of the narrowing between Pt. Postiña and Pt. Cabalar.

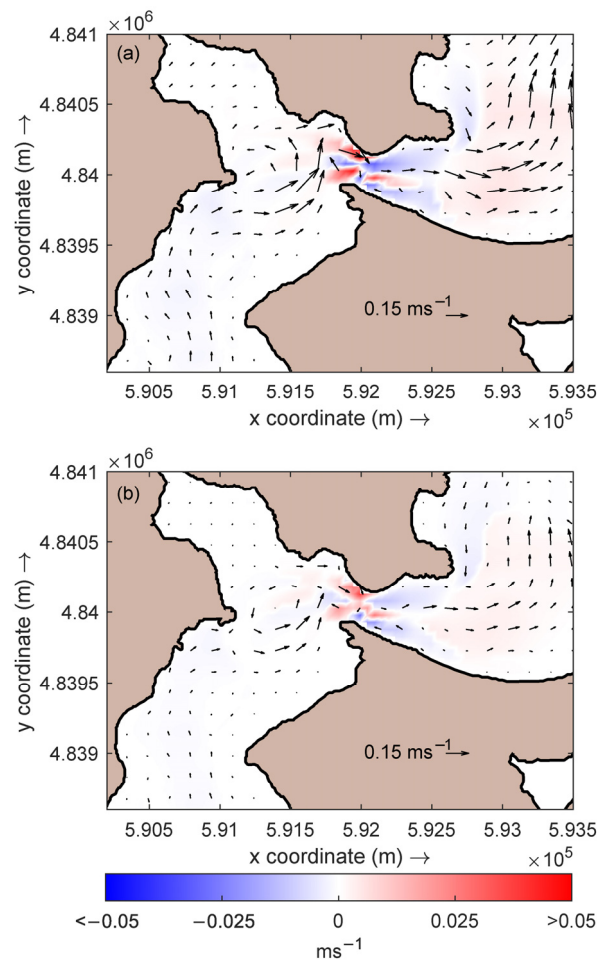


**Figure 13.** Residual flow pattern in Ria de Ortigueira under case study CS8 conditions (vectors); differences in the residual flow magnitude between altered flow and reference situation (CS8–CS4) (colour map). (a) Surface layer; (b) bottom layer.

Finally, CS8 computes the altered residual circulation within the inner Ria de Ortigueira produced by the operation of a bottom-fixed tidal farm under winter riverine and thermohaline conditions along with SW winds. The results obtained (Figure 13) are close, in terms of residual patterns, to those of CS6 in the absence of winds. Likewise, regarding the impacts of the energy extraction on the magnitude of the residual currents, the spatial distribution and magnitude of these impacts present, as in the case of other cases studies conducted (CS5 to CS7), a clear spatial distribution in three different areas (corresponding with the surroundings of the different lines of TSTs), which alternate increments and decrements in residual velocities. Finally, Figure 13 confirms that, in the case of a bottom-fixed tidal farm, a clear reduction in the residual velocity in the surroundings of row 1 is observed and, more specifically, in the central channel of the ria, which is not apparent in the case of a floating plant, as indicated in CS6 (Figure 11).

All in all, it can be established that the operation of the tidal farm proposed in the Ría de Ortigueira only provokes significant alterations in the residual circulation (less than 0.05 ms<sup>-1</sup>) in the area occupied by the farm and in its vicinities (about 150 m distance) regardless of the tidal farm configuration and seasonal scenario considered. These modifications diminish abruptly at some distance from the plant (about 1 km), where they can be neglected. Based on previous results [26], which computed the modifications in the transient circulation in this area with the same plant configuration (both floating and bottom fixed plants), it can be established that the alteration in the magnitude of the residual flow is lower than in the transient circulation and is restricted to a smaller region. This situation contrasts with studies considering a tidal plant occupying the whole water

column, in which the alteration in the residual currents is greater than that in the transient circulation [25].

## 5. Conclusions

In this work, a 3D numerical model was implemented in the Ria de Ortigueira, the westernmost of the Galician Rias Altas (NW Spain), in order to study the potential effects of different configurations of tidal stream farms on the residual circulation, including the estuarine upwelling and its seasonality. First, the model was successfully validated against field measurements obtained by means of an ADCP (Acoustic Doppler Current Profiler) deployed at two different locations in the inner and middle ria during a 19-day period, obtaining correlation coefficients between model and measured data very close to unity. Next, a total of eight case studies (CS) were analysed in order to obtain a detailed seasonality assessment of the impacts of tidal stream energy exploitation on the residual flow. In particular, the unaltered hydrodynamic conditions (absence of tidal farm) and altered conditions (operation of floating and bottom-fixed tidal farms) under typical summer and winter scenarios were analysed, including the absence of wind action and upwelling favourable winds.

The unaltered conditions in the absence of wind action are rather similar under winter and summer conditions. In both cases, two different regions can be distinguished in terms of residual circulation patterns throughout the ria: (i) the inner ria presents similar hydrodynamic patterns throughout the whole water column, with somewhat stronger flow velocities in surface layers, reaching peak velocities of about  $0.25 \text{ ms}^{-1}$  and  $0.15 \text{ ms}^{-1}$  in surface and bottom layers, respectively. On the other hand, the middle and outer ria (ii) are characterized by typical patterns of a positive estuarine circulation.

When the summer SW wind is considered together with summer thermohaline conditions, the resulting circulation follows a conventional two-layer estuarine circulation, reinforcing the residual patterns described above, with similar peak values. However, in the case of a typical winter SW wind, although the resulting circulation pattern is also similar, due to the larger wind velocity and fluvial discharges present, the residual currents induced are stronger, in particular in the surface layer.

Overall, when a tidal farm that partially blocks the water column (either floating or bottom-fixed) operates, the resulting modifications on the residual flow are primarily restricted to the narrowing between Pt. Postiña and Pt. Cabalar in the area occupied by the farm and in its vicinities (roughly over 100–150 m distance) regardless of the combination of tidal farm configuration and boundary conditions selected. The maximum values of the variation in the residual velocities due to the tidal farm operation are of about  $0.05 \text{ ms}^{-1}$  in the influence area of the plant. Outside of this area, the variations on the residual flow magnitude are lower than approx.  $0.01 \text{ ms}^{-1}$  and are virtually negligible at a certain distance from the farm. These results establish that the alteration in the magnitude of the residual flow caused by the operation of a tidal plant either floating or bottom-fixed is lower than alteration in the transient circulation and is restricted to a smaller region. This situation contrasts with studies considering a tidal plant that occupies the entire water column, in which the modification of the residual currents has shown to be greater than in the transient circulation.

In general, and regardless of the combination of tidal farm configuration and hydrodynamic forcing factors, the residual flow velocity increases to the W of the plant and decreases to the E of the plant both in the surface and bottom layers. In addition, in the bottom layer, the magnitude of the effects is quite similar in all the CS considered (bottom or floating plant, with and without wind action) and of less than  $0.03 \text{ ms}^{-1}$ . Although the pattern in the variations in the surface layer is also similar in the four CS, their magnitude is slightly greater when a bottom plant operates in the absence of wind, with increments in the residual flow velocities of around  $0.05 \text{ ms}^{-1}$  at the W of the plant.

This paper determined the potential impact on the residual flows in the Ría de Ortigueira caused by the operation of different tidal stream farms configurations under

different typical hydrodynamic scenarios, establishing that these impacts are restricted to the surroundings of the proposed plants and virtually do not affect the upwelling events, which are of crucial importance in this coastal area. The procedure followed can be used to analyse the potential impacts on the hydrodynamics in other estuaries of interest for a tidal stream energy operation.

**Author Contributions:** Conceptualization, M.S., R.C. and G.I.; methodology, M.S., D.M.F., R.C. and G.I.; software, M.S., D.M.F. and R.C.; validation, M.S., I.L. and R.C.; formal analysis, M.S., I.L. and R.C.; investigation, M.S. and R.C.; resources, M.S., D.M.F., I.L. and R.C.; data curation, M.S., D.M.F., I.L. and R.C.; writing—original draft preparation, M.S. and D.M.F.; writing—review and editing, I.L., R.C. and G.I.; visualization, M.S. and I.L.; supervision, R.C. and G.I.; project administration, R.C. and G.I.; funding acquisition, I.L., R.C. and G.I. All authors have read and agreed to the published version of the manuscript.

**Funding:** This work was supported by the PORTOS project, which is co-financed by the Inter-reg Atlantic Area Programme, through the European Regional Development Fund (grant number EAPA\_784/2018) and “Axudas para a consolidación e estruturación de unidades de investigación competitivas nas universidades do Sistema Universitario Galego (2020–22)” with reference number ED341B 2020/25. During this work, I. López was supported by a postdoctoral grant of the “Programa de Axudas á etapa posdoutoral da Xunta de Galicia”, with reference number ED481D 2019/019.

**Institutional Review Board Statement:** Not applicable.

**Informed Consent Statement:** Not applicable.

**Data Availability Statement:** Not applicable.

**Acknowledgments:** The authors are also grateful for the support of Science Foundation Ireland and MaREI, the Marine Renewable Energy Centre of Ireland, grant SFI MAREI2\_12/RC/2302/P2 Platform RA1b.

**Conflicts of Interest:** The authors declare no conflict of interest.

## References

1. Bekun, F.V.; Alola, A.A.; Sarkodie, S.A. Toward a sustainable environment: Nexus between CO<sub>2</sub> emissions, resource rent, renewable and nonrenewable energy in 16-EU countries. *Sci. Total Environ.* **2019**, *657*, 1023–1029. [CrossRef]
2. Pereira, F.; Neves, M.G.; López-Gutiérrez, J.-S.; Esteban, M.D.; Negro, V. Comparison of Existing Equations for the Design of Crown Walls: Application to the Case Study of Ericeira Breakwater (Portugal). *J. Mar. Sci. Eng.* **2021**, *9*, 285. [CrossRef]
3. Fobissie, E.N. The role of environmental values and political ideology on public support for renewable energy policy in Ottawa, Canada. *Energy Policy* **2019**, *134*, 110918. [CrossRef]
4. Herath, N.; Tyner, W.E. Intended and unintended consequences of US renewable energy policies. *Renew. Sust. Energ. Rev.* **2019**, *115*, 109385. [CrossRef]
5. Nicolli, F.; Vona, F. Energy market liberalization and renewable energy policies in OECD countries. *Energy Policy* **2019**, *128*, 853–867. [CrossRef]
6. Pischke, E.C.; Solomon, B.; Wellstead, A.; Acevedo, A.; Eastmond, A.; De Oliveira, F.; Coelho, S.; Lucon, O. From Kyoto to Paris: Measuring renewable energy policy regimes in Argentina, Brazil, Canada, Mexico and the United States. *Energy Res. Soc. Sci.* **2019**, *50*, 82–91. [CrossRef]
7. Erdiwansyah; Mamat, R.; Sani, M.S.M.; Sudhakar, K. Renewable energy in Southeast Asia: Policies and recommendations. *Sci. Total Environ.* **2019**, *670*, 1095–1102. [CrossRef]
8. European Commission Proposal for a Directive Amending Directive 98/70/EC Relating to the Quality of Petrol and Diesel Fuels and Amending Council Directive 93/12/EC and Amending Directive 2009/28/EC on the Promotion of the Use of Energy from Renewable Sources [COM(2012) 595]. 2012. Available online: <https://eur-lex.europa.eu/legal-content/en/ALL/?uri=CELEX%3A32015L1513> (accessed on 16 October 2022).
9. Portillo Juan, N.; Negro Valdecantos, V.; Esteban, M.D.; López Gutiérrez, J.S. Review of the Influence of Oceanographic and Geometric Parameters on Oscillating Water Columns. *J. Mar. Sci. Eng.* **2022**, *10*, 226. [CrossRef]
10. Bahaj, A.S. Generating electricity from the oceans. *Renew. Sust. Energy Rev.* **2011**, *15*, 3399–3416. [CrossRef]
11. Carballo, R.; Iglesias, G.; Castro, A. Numerical model evaluation of tidal stream energy resources in the Ría de Muros (NW Spain). *Renew. Energy* **2009**, *34*, 1517–1524. [CrossRef]
12. Sánchez, M.; Carballo, R.; Ramos, V.; Iglesias, G. Energy production from tidal currents in an estuary: A comparative study of floating and bottom-fixed turbines. *Energy* **2014**, *77*, 802–811. [CrossRef]



13. Esteban, M.D.; Espada, J.M.; Ortega, J.M.; López-Gutiérrez, J.-S.; Negro, V. What about Marine Renewable Energies in Spain? *J. Mar. Sci. Eng.* **2019**, *7*, 249. [[CrossRef](#)]
14. European Commission. *The Exploitation of Tidal Marine Currents*; EUR16683EN; EC: Brussels, Belgium, 1996.
15. Zarzuelo, C.; López-Ruiz, A.; Díez-Minguito, M.; Ortega-Sánchez, M. Tidal and subtidal hydrodynamics and energetics in a constricted estuary. *Estuar. Coast. Shelf Sci.* **2017**, *185*, 55–68. [[CrossRef](#)]
16. Iglesias, G.; Sánchez, M.; Carballo, R.; Fernández, H. The TSE index—A new tool for selecting tidal stream sites in depth-limited regions. *Renew. Energy* **2012**, *48*, 350–357. [[CrossRef](#)]
17. Fouz, D.M.; Carballo, R.; Ramos, V.; Iglesias, G. Hydrokinetic energy exploitation under combined river and tidal flow. *Renew. Energy* **2019**, *143*, 558–568. [[CrossRef](#)]
18. Liu, Z.; Qu, H.; Shi, H. Numerical study on hydrodynamic performance of a fully passive flow-driven pitching hydrofoil. *Ocean Eng.* **2019**, *177*, 70–84. [[CrossRef](#)]
19. Qian, P.; Feng, B.; Liu, H.; Tian, X.; Si, Y.; Zhang, D. Review on configuration and control methods of tidal current turbines. *Renew. Sustain. Energy Rev.* **2019**, *108*, 125–139. [[CrossRef](#)]
20. Segura, E.; Morales, R.; Somolinos, J.A.; López, A. Techno-economic challenges of tidal energy conversion systems: Current status and trends. *Renew. Sustain. Energy Rev.* **2017**, *77*, 536–550. [[CrossRef](#)]
21. Zhou, Z.; Benbouzid, M.; Charpentier, J.; Scuiller, F.; Tang, T. Developments in large marine current turbine technologies—A review. *Renew. Sustain. Energy Rev.* **2017**, *71*, 852–858. [[CrossRef](#)]
22. Ramos, V.; Carballo, R.; Álvarez, M.; Sánchez, M.; Iglesias, G. Assessment of the impacts of tidal stream energy through high-resolution numerical modeling. *Energy* **2013**, *61*, 541–554. [[CrossRef](#)]
23. Ramos, V.; Carballo, R.; Sanchez, M.; Veigas, M.; Iglesias, G. Tidal stream energy impacts on estuarine circulation. *Energy Conv. Manag.* **2014**, *80*, 137–149. [[CrossRef](#)]
24. Neill, S.P.; Jordan, J.R.; Couch, S.J. Impact of tidal energy converter (TEC) arrays on the dynamics of headland sand banks. *Renew. Energy* **2012**, *37*, 387–397. [[CrossRef](#)]
25. Sánchez, M.; Carballo, R.; Ramos, V.; Iglesias, G. Tidal stream energy impact on the transient and residual flow in an estuary: A 3D analysis. *Appl. Energy* **2014**, *116*, 167–177. [[CrossRef](#)]
26. Sanchez, M.; Carballo, R.; Ramos, V.; Iglesias, G. Floating vs. bottom-fixed turbines for tidal stream energy: A comparative impact assessment. *Energy* **2014**, *72*, 691–701. [[CrossRef](#)]
27. Duarte, P.; Alvarez-Salgado, X.A.; Fernández-Reiriz, M.J.; Piedracoba, S.; Labarta, U. A modeling study on the hydrodynamics of a coastal embayment occupied by mussel farms (Ría de Ares-Betanzos, NW Iberian Peninsula). *Estuar. Coast. Shelf Sci.* **2014**, *147*, 42–55. [[CrossRef](#)]
28. Díez, J. *Las Costas*; Alianza Editorial: Madrid, Spain, 1996.
29. Alvarez, I.; Gomez-Gesteira, M.; de Castro, M.; Novoa, E.M. Ekman transport along the Galician Coast (NW, Spain) calculated from QuikSCAT winds. *J. Mar. Syst.* **2008**, *72*, 101–115. [[CrossRef](#)]
30. Gómez-Gesteira, M.; de Castro, M.; Prego, R.; Pérez-Villar, V. An Unusual Two Layered Tidal Circulation Induced by Stratification and Wind in the Ría of Pontevedra (NW Spain). *Estuar. Coast. Shelf Sci.* **2001**, *52*, 555–563. [[CrossRef](#)]
31. de Castro, M.; Gómez-Gesteira, M.; Alvarez, I.; Lorenzo, M.; Cabanas, J.M.; Prego, R.; Crespo, A.J.C. Characterization of fall-winter upwelling recurrence along the Galician western coast (NW Spain) from 2000 to 2005: Dependence on atmospheric forcing. *J. Mar. Syst.* **2008**, *72*, 145–158. [[CrossRef](#)]
32. Blanton, J.O.; Atkinson, L.P.; Castillejo, F.; Lavin, A. Coastal upwelling off the Rias Bajas, Galicia, Northwest Spain I: Hydrographic Studies. *Réun. Cons. Int. Explor. Mer.* **1984**, *183*, 79–90.
33. Villacieros-Robineau, N.; Herrera, J.L.; Castro, C.G.; Piedracoba, S.; Roson, G. Hydrodynamic characterization of the bottom boundary layer in a coastal upwelling system (Ría de Vigo, NW Spain). *Cont. Shelf Res.* **2013**, *68*, 67–79. [[CrossRef](#)]
34. Alvarez-Salgado, X.A.; Roson, G.; Perez, F.F.; Pazos, Y. Hydrographic variability off the Rias Baixas (NW Spain) during the upwelling season. *J. Geophys. Res.* **1993**, *98*, 14447–14455. [[CrossRef](#)]
35. Souto, C.; Gilcoto, M.; Fariña-Busto, L.; Pérez, F.F. Modeling the residual circulation of a coastal embayment affected by wind-driven upwelling: Circulation of the Ría de Vigo (NW Spain). *J. Geophys. Res.* **2003**, *108*, 4-1–4-18. [[CrossRef](#)]
36. Herrera, J.L.; Rosón, G.; Varela, R.A.; Piedracoba, S. Variability of the western Galician upwelling system (NW Spain) during an intensively sampled annual cycle. *An EOF analysis approach. J. Mar. Syst.* **2008**, *72*, 200–217. [[CrossRef](#)]
37. Prego, R.; Barciela, M.d.C.; Varela, M. Nutrient dynamics in the Galician coastal area (Northwestern Iberian Peninsula): Do the Rias Bajas receive more nutrient salts than the Rias Altas? *Cont. Shelf Res.* **1999**, *19*, 317–334. [[CrossRef](#)]
38. Wooster, W.S.; Bakun, A.; McLain, D.R. Seasonal upwelling cycle along the eastern boundary of the North Atlantic. *J. Mar. Res.* **1976**, *34*, 131–141.
39. Ríos, A.F.; Pérez, F.F.; Fraga, F. Water masses in the upper and middle North Atlantic Ocean east of the Azores. *Deep Sea Res. Part A Oceanogr. Res. Pap.* **1992**, *39*, 645–658. [[CrossRef](#)]
40. Iglesias, G.; Carballo, R. Seasonality of the circulation in the Ría de Muros (NW Spain). *J. Mar. Syst.* **2009**, *78*, 94–108. [[CrossRef](#)]
41. Alvarez, I.; Gomez-Gesteira, M.; de Castro, M.; Gomez-Gesteira, J.L.; Dias, J.M. Summer upwelling frequency along the western Cantabrian coast from 1967 to 2007. *J. Mar. Syst.* **2010**, *79*, 218–226. [[CrossRef](#)]
42. Torres, R.; Barton, E.D.; Miller, P.; Fanjul, E. Spatial patterns of wind and sea surface temperature in the Galician upwelling region. *J. Geophys. Res.* **2003**, *108*, 3130. [[CrossRef](#)]



43. Álvarez-Salgado, X.A.; Labarta, U.; Vinseiro, V.; Fernández-Reiriz, M.J. Environmental drivers of mussels flesh yield in a coastal upwelling system. *Ecol. Indic.* **2017**, *79*, 323–329. [\[CrossRef\]](#)
44. Ospina-Alvarez, N.; Prego, R.; Álvarez, I.; de Castro, M.; Álvarez-Ossorio, M.T.; Pazos, Y.; Campos, M.J.; Bernárdez, P.; Garcia-Soto, C.; Gómez-Gesteira, M.; et al. Oceanographical patterns during a summer upwelling–downwelling event in the Northern Galician Rias: Comparison with the whole Ria system (NW of Iberian Peninsula). *Cont. Shelf Res.* **2010**, *30*, 1362–1372. [\[CrossRef\]](#)
45. Sánchez, M.; Iglesias, G.; Carballo, R.; Fraguera, J.A. Power peaks against installed capacity in tidal stream energy. *IET Renew. Power Gener.* **2013**, *7*, 246–253. [\[CrossRef\]](#)
46. Pugh, D.T. *Tides, Surges, and Mean Sea-Level/a Handbook for Engineers and Scientists*; John Wiley & Sons Inc.: Hoboken, NJ, USA, 1996; p. 486.
47. Cerdeira-Arias, J.D.; Otero, J.; Barceló, E.; Río, G.d.; Freire, A.; García, M.; Nombela, M.Á.; Portilla, G.; Rodríguez, N.; Rosón, G.; et al. Hydrography of shellfish harvesting areas in the western Cantabrian coast (Rías Altas, NW Iberian Peninsula). *Reg. Stud. Mar. Sci.* **2018**, *22*, 125–135. [\[CrossRef\]](#)
48. Iglesias, G.; Carballo, R. Effects of high winds on the circulation of the using a mixed open boundary condition: The Ría de Muros, Spain. *Environ. Modell. Softw.* **2010**, *25*, 455–466. [\[CrossRef\]](#)
49. McClain, C.R.; Chao, S.Y.; Atkinson, L.P.; Blanton, J.O.; de Castillejo, F.F. Wind-driven upwelling in the vicinity of Cape Finisterre, Spain. *J. Geophys. Res.* **1986**, *91*, 8470–8486. [\[CrossRef\]](#)
50. Alvarez, I.; Ospina-Alvarez, N.; Pazos, Y.; de Castro, M.; Bernardez, P.; Campos, M.J.; Gomez-Gesteira, J.L.; Alvarez-Ossorio, M.T.; Varela, M.; Gomez-Gesteira, M.; et al. A winter upwelling event in the Northern Galician Rias: Frequency and oceanographic implications. *Estuar. Coast. Shelf Sci.* **2009**, *82*, 573–582. [\[CrossRef\]](#)
51. Deltares. *User Manual Delft3D-FLOW*; Deltares: Delft, The Netherlands, 2010.
52. Philips, N.A. A co-ordinate system having some special advantages for numerical forecasting. *J. Meteorol.* **1957**, *14*, 184–185. [\[CrossRef\]](#)
53. Carballo, R.; Iglesias, G.; Castro, A. Residual circulation in the Ría de Muros (NW Spain): A 3D numerical model study. *J. Mar. Syst.* **2009**, *75*, 130. [\[CrossRef\]](#)
54. Iglesias, G.; Carballo, R. Can the seasonality of a small river affect a large tide-dominated estuary? The case of the Ría de Viveiro, Spain. *J. Coast. Res.* **2011**, *27*, 1170–1182. [\[CrossRef\]](#)
55. Torres López, S.; Varela, R.A.; Delhez, E. Residual circulation and thermohaline distribution of the Ría de Vigo: A 3-D hydrodynamic model. *Sci. Mar.* **2001**, *65*, 277–289. [\[CrossRef\]](#)
56. Dias, J.M.; Lopes, J.F. Implementation and assessment of hydrodynamic, salt and heat transport models: The case of Ria de Aveiro Lagoon (Portugal). *Environ. Modell. Softw.* **2006**, *21*, 1–15. [\[CrossRef\]](#)
57. Cheng, R.T.; Casulli, V.; Gartner, J.W. Tidal, Residual, Intertidal Mudflat (TRIM) Model and its Applications to San Francisco Bay, California. *Estuar. Coast. Shelf Sci.* **1993**, *36*, 235–280. [\[CrossRef\]](#)
58. Cheng, R.T.; Gartner, J.W. Harmonic analysis of tides and tidal currents in South San Francisco Bay, California. *Estuar. Coast. Shelf Sci.* **1985**, *21*, 57–74. [\[CrossRef\]](#)
59. Smith, S.D. Wind stress and heat flux over the ocean in gale force winds. *J. Phys. Oceanogr.* **1980**, *10*, 709–726. [\[CrossRef\]](#)
60. Yelland, M.J.; Moat, B.I.; Taylor, P.K.; Pascal, R.W.; Hutchings, J.; Cornell, V.C. Wind stress measurements from the open ocean corrected for airflow distortion by the ship. *J. Phys. Oceanogr.* **1998**, *28*, 1511–1526. [\[CrossRef\]](#)
61. Stelling, G.; Leendertse, J. Approximation of convective processes by cyclic ADI methods. In Proceedings of the 2nd ASCE Conference on Estuarine and Coastal Modelling, Tampa, FL, USA, 13–15 November 1992.
62. Chung, T.J. *Computational Fluid Dynamics*; Cambridge University Press: Cambridge, UK, 2002; p. 1012.
63. Rodi, W. Examples of calculation methods for flow and mixing in stratified fluids. *J. Geophys. Res.* **1987**, *92*, 5305–5328. [\[CrossRef\]](#)
64. Defne, Z.; Haas, K.A.; Fritz, H.M. Numerical modeling of tidal currents and the effects of power extraction on estuarine hydrodynamics along the Georgia coast, USA. *Renew. Energy* **2011**, *36*, 3461–3471. [\[CrossRef\]](#)
65. Shapiro, G.I. Effect of tidal stream power generation on the region-wide circulation in a shallow area. *Ocean Sci.* **2011**, *7*, 165–174. [\[CrossRef\]](#)
66. Bahaj, A.S.; Molland, A.F.; Chaplin, J.R.; Batten, W.M.J. Power and thrust measurements of marine current turbines under various hydrodynamic flow conditions in a cavitation tunnel and a towing tank. *Renew. Energy* **2007**, *32*, 407–426. [\[CrossRef\]](#)
67. Álvarez, M.; Ramos, V.; Carballo, R.; López, I.; Fouz, D.M.; Iglesias, G. Application of Marine Spatial Planning tools for tidal stream farm micro-siting. *Ocean Coast. Manag.* **2022**, *220*, 106063. [\[CrossRef\]](#)
68. Myers, L.E.; Bahaj, A.S. An experimental investigation simulating flow effects in first generation marine current energy converter arrays. *Renew. Energy* **2012**, *37*, 28–36. [\[CrossRef\]](#)
69. Umgiesser, G. Modelling the Venice Lagoon. *Int. J. Salt Lake Res.* **1997**, *6*, 177–199. [\[CrossRef\]](#)
70. Salas-de-León, D.A.; Carbajal-Pérez, N.; Monreal-Gómez, M.A.; Barrientos-MacGretor, G. Residual circulation and tidal stress in the Gulf of California. *J. Geophys. Res.* **2003**, *108*, 3317. [\[CrossRef\]](#)